Fluorine-induced d-band center shift of the Nb site boosts anodic formamide electrosynthesis

Fan Dong

dfctbu@126.com

University of Electronic Science and Technology of China https://orcid.org/0000-0003-2890-9964

Shiyong Mou

University of Electronic Science and Technology of China

Siyuan Liu

University of Electronic Science and Technology of China

Weidong Dai

University of Electronic Science and Technology of China

Yanjuan Sun

University of Electronic Science and Technology of China

Article

Keywords:

Posted Date: March 18th, 2024

DOI: https://doi.org/10.21203/rs.3.rs-4079378/v1

Additional Declarations: There is **NO** Competing Interest.

Abstract

Anodic oxidative amidation (EOA) strategies offer a sustainable and potentially promising route for amide synthesis. However, the efficiency and activity of catalysts under oxidative conditions are highly dependent on noble metals. Herein, we present our experimental findings and fundamental understanding that fluorine-doped Nb_2O_5 nanosheet arrays on carbon fiber (F-Nb_2O_5/CP) serve as an efficient and robust non-noble catalyst for the electrochemical synthesis of formamide from ammonia and methanol under ambient conditions. In 0.5 M $KHCO_3$ solution, this catalyst achieved a high Faradaic efficiency of 52.0%, with an N selectivity of 79.1% at 1.5 V versus Hg/HgO electrode. The catalyst exhibited remarkable stability, maintaining its performance over 120 h. By integrating in-situ spectroscopy studies with density functional theory calculations, we revealed that fluorine doping induces a shift in the d-band center of the Nb site. This shift alters the adsorption behavior of OH^- and $^*NH_2$ intermediate on the F-Nb_2O_5 (100) surface, thereby effectively lowering the C-N coupling energy barrier, and boosting the production of formamide.

Introduction

Amide synthesis is crucial due to its extensive applications in biological systems, chemical feedstock, and the pharmaceutical industry.[1,2,3,4] Formamide, the simplest amide, serves as a versatile solvent and building block in chemical synthesis and industrial processes, garnering recent research interest.[4, 5] The traditional reaction for Formamide synthesis often involves fossil-fuel-derived CO, formic acid, and NH_3 under harsh conditions. These synthesis processes require high temperatures and high pressures, resulting in huge energy consumption and CO_2 emissions, leading to environmental concerns.[6,7] Consequently, there is a pressing need for the development of sustainable and efficient methodologies for the synthesis of amide under milder conditions. In response to this, researchers investigated innovative electro-synthetic techniques capable of selectively producing amide products with high energy efficiency, leveraging abundant and renewable feedstocks.[8,9,10,11,12]

The electrochemical synthesis of amide products can be approached in two ways. On one hand, it can be achieved through the cathodic reduction amination route.[8,9,10] On the other hand, anodic oxidative amidation (EOA) strategies present a potentially promising amide synthesis route.[13,14,15,16,17] These strategies offer an alternative to the slow kinetics of the anodic oxygen evolution reaction, a persistent challenge in the field. The exploration and optimization of EOA could pave the way for more efficient and sustainable amide synthesis processes from cost-effective and renewable carbon/nitrogen feedstocks, specifically, methanol and NH_3.[14,16,17,18,19] However, EOA strategies face hurdles, including the durability and activity of catalysts under harsh oxidative conditions, and the dependence on noble metals hinders their practical application. Furthermore, in-situ electrochemical infrared and Raman spectroscopy often rely on noble metal catalysts for surface enhancement, potentially leading to discrepancies in catalyst performance evaluation.[20,21] As such, there is an urgent need to develop non-noble transition metal

catalysts with enhanced activity and stability for EOA strategies, and the ability to enhance in-situ electrochemical spectroscopic signals for capturing key intermediates in mechanistic studies.

Niobium pentoxide (Nb_2O_5), a nontoxic and noteworthy transition metal oxide, is renowned for its unique Lewis and Brønsted acid sites, potent redox ability, and abundant adsorption sites. Its potential applications extend to gas sensors, catalysts, electrochemistry, lithium batteries, and photoelectrodes, which have garnered significant attention in the scientific community.[22,23,24] Furthermore, Nb_2O_5 has shown promise as a non-noble material capable of achieving high sensitivity in surface-enhanced Raman scattering detection applications.[25] Importantly, doping of halide to adjust the electronic configuration has emerged as an effective method to enhance the efficiency and stability of electrocatalysts. Particularly, fluorine doping can effectively alter the electronic structure of active sites, thereby enhancing the durability of electro-oxidation. This stems from fluoride's high electronegativity and low reactivity, which prevent it from easily dissociating from the catalyst surface, thus reducing the loss of active sites.[23,26,27] Recent studies have reported that halide salts can electrochemically increase the active sites of transition metal-based catalysts under alkaline conditions, they have also been identified as effective redox catalysts via paired electrolysis for C-N bond coupling reactions.[28,29,30,31] Consequently, fluorine-doped Nb_2O_5 is expected to serve as an efficient and stable catalyst for the EOA process. Moreover, it shows promise as a substrate for in-situ electrochemical spectroscopy studies.

In this work, we report our experimental and fundamental understanding that fluorine-doped orthorhombic Nb_2O_5 nanosheet arrays on carbon fiber (F-Nb_2O_5/CP) act as an efficient electrocatalyst for the electrochemical formamide synthesis from ammonia and methanol. In 0.5 M $KHCO_3$ solution, this catalyst demonstrated a high Faradaic efficiency of 52.0%, with an N selectivity of 79.1% at 1.50 V versus a Hg/HgO electrode. This performance favorably aligns with the behaviors of most anodic amide electrocatalysts previously reported (Table S1). Key intermediates and products in the reaction process were accurately captured using a series of in-situ and ex-situ detection techniques. Density functional theory calculations reveal that fluorine doping shifts the d-band center of the Nb site, which consequently affects the adsorption behavior of OH^- and $^*NH_2$ intermediate on the F-Nb_2O_5 (100) surface. As a result, it effectively reduces the C-N coupling energy barrier and boosts the production rate of formamide. Our study provides new perspectives into fluorine dopants' role in boosting the activity and stability of Nb_2O_5 and broadens its use as a non-noble semiconductor substrate for surface-enhanced Raman spectroscopy.

Results and discussion

Two forms of orthorhombic Nb_2O_5 (T-Nb_2O_5) were synthesized utilizing the previously reported method.[22, 32] As shown in Fig. 1a, F-Nb_2O_5/CP was derived from the calcination of orthorhombic Nb_3O_7F precursor on carbon fiber under argon conditions. T-Nb_2O_5 nanoparticles on carbon fiber (Nb_2O_5/CP) were synthesized using the same method without HF for comparison. X-ray diffraction spectroscopy (XRD)

results (Fig. 1b) show that the diffraction peaks of F-Nb_2O_5 can be indexed to the orthorhombic Nb_2O_5 phase (PDF 00-030-0873). In comparison, the diffraction peaks of Nb_2O_5 (Supplementary Fig. 1a) were indexed to the orthorhombic Nb_2O_5 phase (PDF 00-027-1003). F-doping slightly shifted the diffraction peaks to lower angles, resulting in the expansion of the crystal lattice. The scanning electron microscopy (SEM) images indicate the well-maintained nanosheet morphologies of F-Nb_2O_5/CP (Fig. 1c, d) after heat treatment of the Nb_3O_7F/CP precursor (Supplementary Fig. 1e, f), with the length of rectangular sheets ranging from 400 to 900 nm and a thickness of around 50 nm. The rectangular sheet structure (Fig. 1e) was further confirmed by transmission electron microscopy (TEM). The high-resolution TEM image (Fig. 1f) shows two groups of lattice fringes with spacings of 0.395 nm and 0.365 nm, in good agreement with the spacings of the (001) and (080) planes of Nb_2O_5, respectively, indicating that these nanoflakes are mostly exposed with the (100) facet.[22] The high-angle annular dark-field scanning transmission electron microscopy (HAADF-STEM) image and Energy dispersive spectroscopy (EDS) elemental mapping results shown in Fig. 1g demonstrate the uniform distribution of Nb, O, and F elements.

The orthorhombic phase and the doped F element of Nb_2O_5 were further confirmed by Raman and X-ray photoelectron spectroscopy (XPS) analysis. Figure 2a depicts the Raman spectrum of F-Nb_2O_5 with the typical Nb–F vibrational band at 132 cm^{-1}. The bands at 230 cm^{-1}, 304 cm^{-1}, and 690 cm^{-1} are attributed to the Nb – O bond stretching vibration, confirming the orthorhombic phase of Nb_2O_5 with F doping.[22,23,33] The band at 994 cm^{-1} was attributed to the peak of the short Nb-O bond, which could enhance the performance of methanol oxidation.[34] In contrast, Fig. 2b exhibits a relatively weak vibrational band at 126 cm^{-1}, indicating the absence of F doping. The bands at 228 cm^{-1}, 309 cm^{-1}, and 689 cm^{-1} also confirm the orthorhombic phase of Nb_2O_5.[35,36,37] The survey XPS spectrum for F-Nb_2O_5 demonstrates that it is composed of F 1s, O 1s, Nb 3p, Nb 3d, and Nb 4p peaks, confirming the doping of the F element (Fig. 2c). The distinct F 1s peak shown in the high-resolution F 1s XPS spectrum (Fig. 2d) at a binding energy of 685.2 eV suggests that the F ion was substituted into the lattice of F-Nb_2O_5. The high-resolution XPS spectrum for O 1s, shown in Fig. 2e, can be fitted into characteristic peaks with binding energies at 530.0 and 532.4 eV. The peak at 530.0 eV is attributed to the Nb – O bond, while the 532.4 eV peak arises due to the existence of loosely bonded oxygen on the surface of Nb_2O_5.[22, 32,32, 38] In the high-resolution Nb 3d XPS spectrum (Fig. 2f), Nb atoms in Nb $3d_{5/2}$ and Nb $3d_{3/2}$ electronic configurations can be observed at 207.8 and 210.6 eV. Moreover, the two small binding energy peaks appearing around 206.5 and 209.2 eV are ascribed to the Nb–F bond.[22, 33] XPS analysis of Nb_2O_5/CP were detailed in Supplementary Fig. 2, which notably demonstrates the absence of the fluorine element. The aforementioned results substantiate the successful fabrication of F-Nb_2O_5/CP, with the (100) facet exposed.

We evaluated the electrocatalytic synthesis of formamide from the co-oxidation of methanol and NH_3 using a two-compartment cell separated by a Nafion117 membrane. The three-electrode system was composed of F-Nb_2O_5/CP or Nb_2O_5/CP as the working electrode, Hg/HgO as the reference electrode, and

a Pt plate as the counter electrode. All potentials are reported versus the Hg/HgO scale unless otherwise noted. All subsequent tests were based on the optimized methanol-to-ammonia ratio, which is a molar ratio of 8:1 (Supplementary Fig. 3). The activity of electrocatalytic formamide synthesis was evaluated by linear sweep voltammetry (LSV) in 0.5 M $KHCO_3$. As shown in Fig. 3a, the current density slightly increased in the presence of 20 mM methanol from the onset potential of 1.2 V, then decreased compared to the LSV curve of 0.5 M $KHCO_3$. This suggests that electrochemical methanol oxidation and water oxidation are competitive reactions on the surface of F-Nb_2O_5/CP. Interestingly, the LSV curve exhibits a sharply increased current density and a low onset potential with the presence of 2.5 mM NH_3 and methanol in the electrolyte, indicating the co-oxidation behavior of methanol and NH_3. Similar trends of competitive reactions, onset potential, and oxidation current density were observed with the Nb_2O_5/CP catalyst, as shown in Supplementary Fig. 4a. Based on the results above, a potential window ranging from 1.2 to 1.9 V was selected for the study of electrocatalytic formamide synthesis. The steady current densities observed in the chronoamperometry curves at different applied potentials (Supplementary Fig. 5) indicate the robust electrochemical oxidation stability of F-Nb_2O_5/CP during the electrocatalytic synthesis tests of formamide.

High-performance liquid chromatography (HPLC) was used for qualitative and quantitative analysis of the electrochemically produced formamide (Supplementary Fig. 6a, b), which was further cross-verified by gas chromatography – mass spectrometry (GC – MS) and 1H-nuclear magnetic resonance (^{1}H NMR, Supplementary Fig. 7). UV – Vis and Ion Chromatography (IC) were employed for the detection of byproducts such as H_2O_2 (Supplementary Fig. 6c, d), $HCOO^-$, NO_2^-, and NO_3^-. The Faradaic efficiency, product distribution, and yield of formamide show a volcano-like trend (Fig. 3b) as the applied potential increases from 1.2 to 1.9 V. The FEformamide on F-Nb_2O_5/CP achieves 52.0%, with a yield of 252 μmol cm^{-2} h^{-1} at − 1.5 V. Meanwhile, the selectivity of N and C, calculated from the consumption of NH_3 and methanol (Supplementary Fig. 8), are 79.1% and 20.5% respectively. The FEformamide and yield on Nb_2O_5/CP achieve 25.6%, with a yield of 96 μmol cm^{-2} h^{-1} at − 1.6 V (Supplementary Fig. 4b). An isotope-labeled experiment was performed to validate the origin of the formamide products. Figure 4c displays the total ion chromatography (TIC) of formamide and ^{15}N-labeled formamide, where the N source was NH_3 and $^{15}NH_3$. Correspondingly, the mass spectra of ^{15}N-labeled formamide (m/z = 46) rise more sharply than that of the formamide, as depicted in Fig. 3d, thereby proving the N source of formamide. Moreover, no TIC signals from other organic compounds were observed, indicating that the product of the C–N coupling reaction is formamide on F-Nb_2O_5/CP. Control experiments were conducted to validate the reaction pathway. Initially, a significant increase in both the yield and Faraday efficiency (94%) of formamide was observed when formaldehyde was used as a substitute for the carbon source (Fig. 3e). This finding suggests that the aldehyde intermediate, derived from methanol, plays a pivotal role in the C-N coupling process. However, when NH_2OH was substituted for the NH_3 feedstock, there was a marked reduction in both the yield and Faraday efficiency of formamide. This indicates that NH_2OH may not act as a key intermediate in the reaction. Furthermore, in a 0.5 M NaOH solution, there is a

noticeable decrease in both the Faraday efficiency and yield of formamide. This can be ascribed to the competitive reaction that involves nucleophilic reagents, namely, OH^- and NH_3 derivatives, indicating that C-N coupling may proceed through a nucleophilic attack process. [13] The results of the long-term stability test are shown in Fig. 4f, where both the current density and FEformamide remain steady over 120 hours. The long-term stability of the F-Nb_2O_5/CP catalysts after the test, as confirmed by XPS (Supplementary Fig. 9), XRD, and SEM analyses (Supplementary Fig. 10), indicating the robust electrochemical oxidation stability for the anodic formamide synthesis.

Studies have indicated that the adsorption of halogen ions is potential dependence, where reactions between these ions and adsorbed species produce oxidation-resistant compounds, even at high anodic potentials.[39,40] Fig. 3g displays that the FEformamide on Nb_2O_5/CP was effectively increasing when 10 mM of fluoride or chloride ions were added to the solution. Conversely, after the addition of 10 mM bromide or iodide ions to the solution, the $FE_{formamide}$ sharply decreases. Thus, it can be concluded that fluoride and chloride ions appear to facilitate the anodic amide synthesis process. To evaluate whether the performance of catalysis is influenced by the electrochemically active surface area (ECSA) of F-Nb_2O_5/CP and Nb_2O_5/CP, we conducted measurements of the double-layer capacitance (Cdl). Supplementary Fig. 11a and 11b display the cyclic voltammograms (CVs) of F-Nb_2O_5/CP and Nb_2O_5/CP at various scan rates (10–100 mV s^{-1}), respectively. As shown in Fig. 3h, the Cdl of F-Nb_2O_5/CP (3.9 mF cm^{-2}) is nearly equivalent to but marginally lower than that of Nb_2O_5/CP (4.3 mF cm^{-2}). This suggests that F-Nb_2O_5/CP possesses a slightly smaller ECSA. Furthermore, Nb_2O_5/CP exhibits lower charge transfer resistance in the Nyquist plots (Fig. 3i). Hence, it can be inferred that the contribution to the C-N bond formation activity is not derived from the ECSA or the catalyst's impedance. Instead, it primarily stems from the doping of fluorine.

Given the fact that Nb_2O_5 nanoparticles have been identified as a promising non-noble semiconductor for surface-enhanced Raman substrates, capturing the reaction intermediates using in-situ Raman spectroscopy on F-Nb_2O_5/CP is of interest. As displayed in Fig. 4a, the in-situ Raman spectra of F-Nb_2O_5/CP were captured under operando conditions at various operating potentials. As the applied potential escalated from the open circuit potential (OCP) to 1.9 V, significant peaks centered at 1336 cm^{-1} and 1580 cm^{-1} emerged on F-Nb_2O_5/CP. These peaks correspond to the stretching vibrations of the C–N and NH_2, thereby affirming the presence of the $^*NH_2$ intermediate and the formation of the C–N bond.[20,41] To further reveal the changes in reaction intermediates, we performed in-situ electrochemical attenuated total reflection surface-enhanced infrared absorption spectroscopy (ATR-SEIRAS). The in-situ IR spectra signals of F-Nb_2O_5/CP ranged from OCP to 1.9 V (Fig. 4b). The characteristic IR peaks of the amide were successfully traced as the potential changed. The spectral features in the wavenumber region of 2900–3400 cm^{-1} are identified as $\nu(NH_2)$, corresponding to the amide A bands (typically found within the 3300–3500 cm^{-1} range). Notably, the emergence of new bands at 1631, 1498, and 1238 cm^{-1} can be observed. These bands can be respectively classified as the amide I band (generally within the 1600–

1800 cm^{-1} range), the amide II band (typically within the 1470–1570 cm^{-1} range), and the amide III bands (usually found within 1250 to 1350 cm^{-1} range)., which can be assigned to $\delta(NH_2)$, v(C = O), and v(C – N) of adsorbed formamide.[42] The key intermediate species of $^*CHO$ and $^*CH_2O$ were successfully detected at 1366 and 1418 cm^{-1}, respectively. This observation aligns with the electrocatalytic C–N bond coupling processes that lead to the production of formamide, achieved through the coupling of $^*CH_2O/^*CHO$ with $^*NH_2$ intermediates.

To gain further insights into the electrocatalytic C–N bond coupling process, online differential electrochemical mass spectrometry (DEMS) was employed. Importantly, an experiment utilizing ^{15}N-labeled NH_3 was conducted to differentiate between the anodic formation of N_2 and CO during the reaction, given their identical mass-charge ratio of 28. As shown in Fig. 4c, the potential-dependent mass signals of m/z = 44, assigned to CO_2, and m/z = 28, assigned to CO, were observed during the LSV scan. Interestingly, the intensities of the m/z = 29, m/z = 30, assigned to $^{15}N_2$, and m/z = 31 peaks are negligible in our test (Fig. 4d). This deviates from the DEMS test results reported in previous literature on formamide electrochemical synthesis, suggesting that our reaction may involve distinct reaction intermediates and pathways. The intensity of the m/z = 32 peak can be ascribed to the competitive oxygen evolution reaction. It is also noteworthy that the intensity of mass signals of m/z = 33 and m/z = 34, attributed to $^{15}NH_2OH$, is quite faint, implying that it may not be a key intermediate. The potential-dependent mass signals of m/z = 45 and m/z = 46 can be respectively attributed to the formation of formamide and ^{15}N-labeled formamide. From the results, we can deduce the following. Firstly, ammonia does not readily oxidize to nitrogen, nitrite, and nitrate on the surface of F-Nb_2O_5, indicating that $^*NH_2$, derived from the dehydrogenation of NH_3, serves as the key intermediate. Secondly, the oxidation products of methanol primarily comprise CO and CO_2, with trace amounts of formic acid, suggesting the existence of an aldehyde intermediate. It can be postulated that the yield of in-situ aldehyde intermediates may be a limiting factor in the production rate of formamide.

To extract a further level of insights into the formamide electro-synthetic pathways, DFT calculations, and AIMD calculations were implemented on F-Nb_2O_5 (100) and Nb_2O_5 (100) surfaces toward electro-formamide synthesis. The Gibbs free energy change during the C-N coupling reaction was meticulously analyzed. Figure 5a and 5b illustrate the first pathway for the electro-synthesis of formamide on F-Nb_2O_5 (100) and Nb_2O_5 (100), respectively. The corresponding atomic configurations are depicted in the Supplementary Figs. 13 and 14. A thermodynamically viable path was identified for the production of an aldehyde intermediate, following the sequence $CH_3OH^* \rightarrow CH_3O^* \rightarrow CH_2O^*$. The formation of CH_3O^* is an uphill process on both catalysts, but it is more favorable on F-Nb_2O_5 (100) with an energy barrier of 0.12 eV. It is noteworthy that the formation of $^*NH_2$ on F-Nb_2O_5 (100) is a downhill process with an energy barrier of 0.12 eV. This is in stark contrast to the process on Nb_2O_5 (100), which is an uphill process and has a significantly higher energy barrier of 1.01 eV. Initially, the C-N bond is formed via the nucleophilic attack of the $^*NH_2$ intermediate on the $^*CH_2O$ intermediate. Subsequently, the resulting $^*NH_2CH_2O$

intermediate undergoes a dehydrogenation step to produce formamide. A transition state search was conducted to further investigate the differences in electrocatalytic performance. The findings reveal that F-Nb_2O_5 presents a lower kinetic barrier, with an energy of 0.29 eV. The formation of the C-N bond process and free energy change have been corroborated by the results of the restrictive molecular dynamics slow growth simulation (Supplementary Fig. 15a, b). In contrast, the C-N coupling barrier for Nb_2O_5 is considerably high at 0.97 eV. The intermediate is more predisposed to dehydrogenate to $^*CHO$, as opposed to C-N coupling. The $^*NH_2$ tends to extract H from $^*CH_2O$, forming adsorbed $^*NH_3$, which exhibits a catalyst-like behavior. This could serve as one explanation for the high nitrogen selectivity and low carbon selectivity observed on the Nb_2O_5 catalyst. Ultimately, the desorption barrier of formamide from the surface of the F-Nb_2O_5 catalyst is 0.02 eV lower than that of the Nb_2O_5 surface.

Supplementary Fig. 12 a and b illustrate the second pathway, which involves the formation of a C-N bond via a nucleophilic attack between the $^*NH_2$ and $^*CHO$ intermediates on F-Nb_2O_5 (100) and Nb_2O_5 (100). The corresponding atomic configurations are depicted in the Supplementary Figs. 16 and 17. F-Nb_2O_5 (100) presents a lower barrier of 0.24 eV compared to the first pathway. However, $^*CHO$ tends to be preferentially oxidized to CO products, as identified by the slow growth simulation (refer to Supplementary Fig. 14c, and 14d), and the production of CO was confirmed by the DEMS results. In contrast, the barrier for $^*CHO$ and $^*NH_2$ coupling on the Nb_2O_5 surface is only 0.12 eV. This process, however, is hindered by the dehydrogenation step of $^*NH_3$, which has a significantly higher barrier of 1.01 eV. To ascertain whether the C-N coupling process pathway involves a nucleophilic attack, we performed an electrostatic potential (ESP) analysis of the $^*NH_2$ + $^*CH_2O$ process (Fig. 5c). The analysis revealed that $^*CH_2O$ possesses an electrophilic carbon center, which subsequently undergoes a nucleophilic attack by the adjacent $^*NH_2$. Ultimately, the thermodynamically favorable reaction pathway on F-Nb_2O_5 (100) was unveiled, as depicted in Scheme 1. This pathway involves the nucleophilic attack of the ammonia-derived $^*NH_2$ on the methanol-derived $^*CH_2O$, followed by a dehydrogenation process to form formamide.

To further investigate the contribution of F-doping to the C-N coupling process, we performed a computational analysis of the electronic structural properties at the Nb sites. Figure 5d displays the projected density of states (PDOS) of the d orbitals of the Nb sites, confirming a significant downshift in the band center of the F-doped Nb site, from 0.507 eV to -1.659 eV, which could significantly impact the electrochemical reaction performance. Given the significance of OH^- adsorption under alkaline conditions, Fig. 5e presents the Crystal Orbital Hamilton Population (COHP) analysis results of the adsorbed OH^- intermediate on the surfaces of F-Nb_2O_5 (100) and Nb_2O_5 (100). The findings suggest that OH^- adsorption is more thermodynamically favorable on F-Nb_2O_5 (100), primarily due to the contribution of single-electron adsorption. This is confirmed by differential charge density results (Supplementary Fig. 18), which show that the Nb site adjacent to the F element, exhibiting an electron-deficient state, is a significant contributor. As illustrated in Fig. 5f, the COHP results of the adsorbed $^*NH_2$ intermediate suggest that the $^*NH_2$ intermediate exhibits greater stability on the F-Nb_2O_5 (100) surface, which is

evidenced by the relationship between the adsorption energy and ICOHP data. The interaction between the pz orbital of the adsorbed $^{*}OH$ and $^{*}NH_2$ intermediate, and the dz2 orbital of Nb, plays a significant role in the formation of the Nb-O and Nb-N bonds, respectively. This could be a crucial factor in understanding the adsorption strength on metal surfaces, particularly in the context of back-donation interactions. Interestingly, the COHP results of the adsorbed $^{*}CH_2O$ (Supplementary Fig. 19) show that the Nb-O bond originates from the contribution of O 2p and Nb 5s. On the F-Nb_2O_5 (100) surface, $^{*}CH_2O$ shows stable and moderate adsorption energy, not affected by the downshift of the d-band center. These results are in accordance with the Sabatier principle, which states that an effective catalyst should demonstrate a moderate binding strength with the reactants.[43,44] Therefore, by elucidating the mechanism of fluorine doping in boosting C-N coupling, we can conclude that F-Nb_2O_5 (100) is more favorable for the electrochemical anodic formamide synthesis.

Conclusion

In conclusion, our study demonstrates that F-doped orthorhombic Nb_2O_5 nanosheet arrays on carbon fiber paper (F-Nb_2O_5/CP) serve as an effective and robust electrocatalyst for the electrochemical synthesis of formamide from ammonia and methanol. Achieving a high Faradaic efficiency of 52.0% and an N selectivity of 79.1% at 1.50 V vs. Hg/HgO electrode in a 0.5 M $KHCO_3$ solution. Our in-situ and ex-situ detection methodologies have effectively pinpointed key intermediates and products within the reaction process, thereby contributing to a fundamental comprehension of the reaction pathway. Fluorine doping not only enhances the electrochemical oxidation stability and activity for anodic formamide synthesis but also, as revealed by density functional theory calculations, induces a downshift in the d-band center of the Nb site, which consequently affects the adsorption behavior of OH^{-} and $^{*}NH_2$ intermediates on the F-Nb_2O_5 (100) surface. As a result, it effectively reduces the C-N coupling energy barrier and boosts the production rate of formamide. Our work provides new perspectives on the role of fluorine dopants in enhancing the activity and stability of Nb_2O_5, and expanding its application scope when utilized as a non-noble semiconductor substrate for surface-enhanced Raman spectroscopy.

Methods

Materials Synthesis

Synthesis of F-Nb_2O_5 nanosheets on carbon nanofiber paper (F-Nb_2O_5/CP). In a typical synthesis, 0.15 g Nb powder, and 0.3 mL HF was added into 30 mL distilled water, and the mixture solution was transferred into a 50 mL Teflon-lined autoclave containing a 2×3 cm carbon nanofiber paper and kept in an oven at 180 ºC for 12 h. The obtained Nb_3O_7F nanosheets on carbon fiber paper (Nb_3O_7F/CP) precursor solid was washed thoroughly with deionized water and dried at 80 ºC overnight. The as-prepared Nb_3O_7F/CP precursor was annealed at 600 ºC for 1 h in air to obtain F-Nb_2 O $_5$/CP.

Synthesis of Nb_2O_5 nanoparticles on carbon nanofiber paper (Nb_2O_5/CP) was synthesized by a hydrothermal method from niobium oxalate. In a typical synthesis, 0.8 g niobium oxalate was added into 30 mL distilled water, the mixture solution was transferred into a 50 mL Teflon-lined autoclave containing a 2×3 cm carbon fiber paper and kept in oven at 180 ºC for 12 h. Then precursor was annealed at 600 ºC for 1 h in air to obtain Nb_2O_5/CP.

Materials Characterization

XRD patterns were obtained from a Shimazu XRD-6100 diffractometer with Cu Kα radiation (40 kV, 30 mA) of wavelength 0.154 nm (Japan). Scanning electron microscopy (SEM, Gemini SEM 30), high-resolution transmission electron microscopy (HRTEM, Tecnai F30), X-ray photoelectron spectroscopy (XPS, ESCALAB250Xi), and Horiba XploRA PLUS Raman spectrometer were used to characterize the structure and composition of the catalysts.

Electrochemical measurements

Before tests, the Nafion proton exchange membrane was pretreated by heating in 3% H_2O_2 solution, 0.5 M H_2SO_4 and ultrapure water at 80°C for 1 h, respectively. Electrochemical measurements were performed on a CHI 760D electrochemical analyzer (CHI Instruments, Inc., Shanghai) in a standard three-electrode system using F-Nb_2O_5/CP or Nb_2O_5/CP as working electrode, Hg/HgO as reference electrode, and Pt foil as counter electrode. Polarization curves were obtained using LSV with a scan rate of 5 mV s^{-1}. The long-term durability test was performed using chronopotentiometric measurements.

Detection and quantification of possible products

Detection and quantification of formamide were performed on Shimadzu HPLC with SPD-M40 photodiode array detector using 4.6 × 250 mm C18 Superb 5um column, 90:10 water-acetonitrile solution was used as the mobile phase. Further cross-verified of formamide was performed on an Agilent 7890 gas chromatograph system equipped with mass detectors, and a headspace autosampler (ColinTech), the separation was achieved using a DB-624 column (100% polyethylene glycol, 60 m long with a 0.25 mm i.d. and 1.0 µm film thickness),^{1}H nuclear magnetic resonance (NMR) spectra were collected on a superconducting-magnet NMR spectrometer (BRUKER AscendTM 600 MHz) and dimethyl sulphoxide was used as an internal to calibrate the chemical shifts in the spectra. Detection and quantification of $HCOO^-$, NO_2^-, and NO_3^- were performed on the Shimadzu ion chromatograph system with a CDD-10A VP conductivity detector. The H_2O_2 concentration in the electrolyte was determined using a Shimadzu UV-2600 UV spectrophotometer by potassium titanium oxalate method with a maximum response at 400 nm.

FE was determined using the following equation:

FE = Amount of electrons required to form the products/Total amount of electrons supplied to the system×100%

In-situ Raman tests

For in-situ Raman experiments, in situ, Raman spectroscopy was conducted on a Horiba XploRA PLUS Raman spectrometer. The in-situ experiments were conducted with a custom-made electrochemical cell with Pt foil as the counter electrode and Hg/HgO as reference electrode. The excitation wavelength was 638 nm and a 50 × microscope objective with a numerical aperture of 0.55 was used. The spectra of the preconditioned electrode at each applied potential were collected for 60 seconds.

In situ ATR SEIRAS

A typical reactor of ATR-SEIRAS consists of two chambers with three electrodes. For the working electrode, 20 uL catalyst ink (5 mg mL^{-1}) was dropped onto the Si crystal, and dried in air before a test. Platinum sheet and Hg/HgO electrode were used as the counter and reference electrodes, respectively. 0.5 M $KHCO_3$ electrolyte were injected into anode and cathode chamber, respectively. An INVENIO R FT-IR (Bruker) spectrometer equipped with a liquid nitrogen cooled mercury cadmium telluride detector was used for the in-situ ATR-SEIRAS test and all spectra were given by the absorbance ($-\log(R/R_0)$). The spectral resolution was 4 cm^{-1} and the scanning time was 0.5 min for each curve. The potential-dependent ATR-SEIRAS was carried out with the chronoamperometry test from 1.2 V to 1.9 V (vs.Hg/HgO).

Online differential electrochemical mass spectrometry (DEMS) measurement

Online DEMS was carried out to detect the volatile matters during the real-time electrolysis process (Shanghai Linglu Instrument & Equipment Co). The signal was collected through a hydrophobic polytetrafluoroethylene (PTFE) membrane. The electrolysis reaction occurred on one side of the PTFE membrane and the produced volatile matter was brought to the other side through a pump. The potential-dependent Online DEMS was carried out with the LSV test from 1.0 V to 1.9 V (vs.Hg/HgO) with a scan rate of 10 mV s^{-1}.Sequentially, those matters were detected by mass spectrometry.

Computational details

The spin-polarized first-principles calculations based on the Density Functional Theory (DFT) were performed using the Vienna Ab initio Simulation Package (VASP).[45,46,47] The Perdew-Burke-Ernzerhof (PBE) exchange-correlation functional within the generalized gradient approximation (GGA) was employed to describe the exchange-correlation energy.[48] The projector-augmented-wave (PAW) method was adopted for the pseudopotentials.[49] The energy cutoff for the plane wave basis expansion was set to 500 eV. The force on each atom was set as 0.02 eV $Å^{-1}$ for the convergence criterion. The (100)

surface of Nb_2O_5 was used to investigate the anodic formamide electro-synthesis performance. The slab model was constructed in a four-layer 2×3 (100) surface, with a vacuum layer of 15 Å in the z direction to avoid the interaction between layers. The sampling in the Brillouin zone was set with 3×3×1 by the Monk Horst-Pack method.[50] The van der Waals interaction was considered by using the DFT-D3 method. The free energies of the anodic formamide electro-synthesis steps were calculated using the equation: $\triangle G=\triangle E_{DFT}+\triangle E_{ZPE}-T_{\Delta S}$, where $\triangle E_{DFT}$ is the DFT energy difference, the $\triangle E_{ZPE}$, and $T_{\Delta S}$ are obtained by the zero-point energy correction and analysis of the variation of entropy, respectively. We conducted an ab initio molecular dynamics (AIMD) simulation at 300 K and constructed the corresponding free energy profiles. The simulation utilized a time step of 0.5 fs, with the convergence criteria for each electronic step set to 1×10^{-6} eV, using the gamma point of the Brillouin zone using a Nose-Hoover thermostat. The free energy profile for this reaction was obtained using the slow-growth method, employing a step size of 0.0005 Å. Crystal Orbital Hamilton Population (COHP) analysis was performed with the LOBSTER code.[51]

Declarations

Data availability

The data that support the findings of this study are available within the article and its Supplementary Information files or from the corresponding author upon reasonable request.

AUTHOR INFORMATION

*Corresponding Author

dongfan@uestc.edu.cn, dfctbu@126.com (Fan Dong).

Conflict of interest

The authors declare that they have no conflict of interest.

Acknowledgments

This work was supported by the National Key R&D Project of China (Grant No. 2020YFA0710000), National Natural Science Foundation of China (Grant Nos. 22225606, 22276029).

References

1. Pattabiraman VR, Bode JW. Rethinking amide bond synthesis. *Nature* **480**, 471-479 (2011).
2. Kim JE, Choi S, Balamurugan M, Jang JH, Nam KT. Electrochemical C–N Bond Formation for Sustainable Amine Synthesis. *Trends Chem.* **2**, 1004-1019 (2020).
3. Li J, Zhang Y, Kuruvinashetti K, Kornienko N. Construction of C-N bonds from small-molecule precursors through heterogeneous electrocatalysis. *Nat. Rev. Chem.* **6**, 303-319 (2022).

4. Peng X, et al. Electrochemical C-N coupling of CO_2 and nitrogenous small molecules for the electrosynthesis of organonitrogen compounds. *Chem. Soc. Rev.* **52**, 2193-2237 (2023).
5. Seavill PW, Wilden JD. The preparation and applications of amides using electrosynthesis. *Green Chem.* **22**, 7737-7759 (2020).
6. Zhang YJ, Dai XC, Wang HL, Shi F. Catalytic Synthesis of Formamides with Carbon Dioxide and Amines. *Acta Physico-Chimica Sinica* **34**, 845-857 (2018).
7. Frogneux X, Jacquet O, Cantat T. Iron-catalyzed hydrosilylation of CO: CO conversion to formamides and methylamines. *Catal.Sci. Technol.* **4**, 1529-1533 (2014).
8. Lan J, et al. Efficient electrosynthesis of formamide from carbon monoxide and nitrite on a Ru-dispersed Cu nanocluster catalyst. *Nat. Commun.* **14**, 2870 (2023).
9. Li J, Kornienko N. Electrochemically driven C-N bond formation from CO_2 and ammonia at the triple-phase boundary. *Chem. Sci.* **13**, 3957-3964 (2022).
10. Guo C, et al. Electrochemical Upgrading of Formic Acid to Formamide via Coupling Nitrite Co-Reduction. *J. Am. Chem. Soc.* **144**, 16006-16011 (2022).
11. Ye Y, Li Z, Ding S, Fu J, Liu H, Zhu W. Synergistic treatment of carbon dioxide and nitrogen-containing wastewater by electrochemical C-N coupling. *iScience* **26**, 107009 (2023).
12. Jouny M, et al. Formation of carbon-nitrogen bonds in carbon monoxide electrolysis. *Nat. Chem.* **11**, 846-851 (2019).
13. Lu Y, et al. Anodic Electrosynthesis of Amide from Alcohol and Ammonia. *CCS Chem.* **6**, 125-136 (2024).
14. Zhu J, et al. Formamide Electrosynthesis from Methanol and Ammonia in Water over Pr-Doped MnO_2. *JACS Au* **3**, 2987-2992 (2023).
15. Jin M, et al. Electrosynthesis of N.N-dimethylformamide from market-surplus trimethylamine coupled with hydrogen production. *Green Chem.* **25**, 5936-5944 (2023).
16. Shao J, et al. Scalable Electrosynthesis of Formamide through C-N Coupling at the Industrially Relevant Current Density of 120 mA cm^{-2}. *Angew. Chem., Int. Ed.* **61**, e202213009 (2022).
17. Meng N, et al. Electrosynthesis of formamide from methanol and ammonia under ambient conditions. *Nat. Commun.* **13**, 5452 (2022).
18. Natte K, Neumann H, Beller M, Jagadeesh RV. Transition-Metal-Catalyzed Utilization of Methanol as a C(1) Source in Organic Synthesis. *Angew. Chem., Int. Ed.* **56**, 6384-6394 (2017).
19. Olah GA. Beyond oil and gas: the methanol economy. *Angew. Chem., Int. Ed.* **44**, 2636-2639 (2005).
20. Schlucker S. Surface-enhanced Raman spectroscopy: concepts and chemical applications. *Angew. Chem., Int. Ed.* **53**, 4756-4795 (2014).
21. Bell SEJ, et al. Towards Reliable and Quantitative Surface-Enhanced Raman Scattering (SERS): From Key Parameters to Good Analytical Practice. *Angew. Chem., Int. Ed.* **59**, 5454-5462 (2020).

22. Liu X, et al. F-doped orthorhombic Nb_2O_5 exposed with 97% (100) facet for fast reversible Li^+-Intercalation. *Green Energy & Environment*, (2022), https://doi.org/10.1016/j.gee.2022.09.009.
23. Ishikawa S, et al. Synthesis of Fluoride-Containing High Dimensionally Structured Nb Oxide and Its Catalytic Performance for Acid Reactions. *Inorg. Chem.* **59**, 9086-9094 (2020).
24. Hirunsit P, Toyao T, Siddiki S, Shimizu K, Ehara M. Origin of Nb_2O_5 Lewis Acid Catalysis for Activation of Carboxylic Acids in the Presence of a Hard Base. *Chemphyschem* **19**, 2848-2857 (2018).
25. Shan YF, et al. Niobium pentoxide: a promising surface-enhanced Raman scattering active semiconductor substrate. *npj Comput. Mater* **3**, 11 (2017).
26. Zhang A, Liang Y, Zhang H, Geng Z, Zeng J. Doping regulation in transition metal compounds for electrocatalysis. *Chem. Soc. Rev.* **50**, 9817-9844 (2021).
27. Fan X, et al. Defect-enriched iron fluoride-oxide nanoporous thin films bifunctional catalyst for water splitting. *Nat. Commun.* **9**, 1809 (2018).
28. Dinh KN, Chatti M, Nguyen TD, Hoogeveen DA, MacFarlane DR, Simonov AN. A Universal Saline-Alkaline Etching Procedure to Enhance the Activity of Oxygen Evolution Catalysts. *ACS Energy Lett.* **7**, 3910-3916 (2022).
29. Fiori IA, Melle GB, Sitta E. Halide adsorption effect on methanol electro-oxidation reaction studied by dynamic instabilities. *J. Electroanal. Chem.* **856**, (2020).
30. Liang S, Zeng CC, Tian HY, Sun BG, Luo XG, Ren FZ. Electrochemically Oxidative alpha-C-H Functionalization of Ketones: A Cascade Synthesis of alpha-Amino Ketones Mediated by NH_4I. *J. Org. Chem.* **81**, 11565-11573 (2016).
31. Kang L-S, Luo M-H, Lam CM, Hu L-M, Little RD, Zeng C-C. Electrochemical C–H functionalization and subsequent C–S and C–N bond formation: paired electrosynthesis of 3-amino-2-thiocyanato-α,β-unsaturated carbonyl derivatives mediated by bromide ions. *Green Chem.* **18**, 3767-3774 (2016).
32. Liu M, Yan C, Zhang Y. Fabrication of Nb_2O_5 nanosheets for high-rate lithium ion storage applications. *Sci. Rep.* **5**, 8326 (2015).
33. Jin FX, Ma XJ, Guo SQ. F-doped hierarchical Nb2O5: Structural, optical and photocatalytic performance. *Mater. Lett.* **347**, 134664 (2023).
34. Wang XL, et al. Raman unveiled Nb-O-bond-dependency selectivity for methanol electro-oxidation at high current density. *Appl. Catal. A Gen.* **664**, 119341 (2023).
35. Liu F, et al. Dense T-Nb_2O_5/Carbon Microspheres for Ultrafast-(Dis)charge and High-Loading Lithium-Ion Batteries. *ACS Appl Mater Interfaces* **14**, 49865 (2022).
36. Li N, et al. Precisely Tunable T-Nb_2O_5 Nanotubes via Atomic Layer Deposition for Fast-Charging Lithium-Ion Batteries. *ACS Appl Mater Interfaces* **13**, 16445-16453 (2021).
37. Kong L, Zhang C, Wang J, Qiao W, Ling L, Long D. Nanoarchitectured Nb_2O_5 hollow, Nb_2O_5@carbon and NbO_2@carbon Core-Shell Microspheres for Ultrahigh-Rate Intercalation Pseudocapacitors. *Sci. Rep.* **6**, 21177 (2016).

38. Wu YL, et al. Fluorine substitution enabling pseudocapacitive intercalation of sodium ions in niobium oxyfluoride. *J. Mater. Chem. A* **7**, 20813-20823 (2019).
39. Kikuchi M, Mukouyama Y, Okamoto H. Chloride ion influencing potential oscillation generated by formaldehyde oxidation. *Electrochim. Acta* **53**, 7817-7824 (2008).
40. Sobkowski J, Wieckowski A. The influence of halide ions on methanol adsorption and oxidation on a platinized electrode. *J. Electroanal. Chem. Interfacial. Electrochem.* **41**, 373-379 (1973).
41. Signorile M, Pantaleone S, Balucani N, Bonino F, Martra G, Ugliengo P. Monitoring the Reactivity of Formamide on Amorphous SiO_2 by In-Situ UV-Raman Spectroscopy and DFT Modeling. *Molecules* **25**, 2274 (2020).
42. Ji Y, et al. DFT-Calculated IR Spectrum Amide I, II, and III Band Contributions of N-Methylacetamide Fine Components. *ACS Omega* **5**, 8572-8578 (2020).
43. Medford AJ, et al. From the Sabatier principle to a predictive theory of transition-metal heterogeneous catalysis. *J. Catal.* **328**, 36-42 (2015).
44. Zhu X, Li Y. Insights into the Structure-Sensitive Catalytic Performance of Palladium–Copper Alloys in Electrochemical Urea Synthesis. *ACS. Catal.* **13**, 15322-15330 (2023).
45. Kresse, Georg, and Jürgen Furthmüller. Efficiency of ab-initio total energy calculations for metals and semiconductors using a plane-wave basis set. *Comput. Mater. Sci.* **6**,15-50 (1996).
46. Kozlov, Almudena Notario-Estévez Sergey M., Francesc Viñes, and Francesc Illas. Electronic-structure-based chemical descriptors:(in) dependence on self-interaction and Hartree-Fock exchange. *Phy. Rev. B* **54**.11169-11186 (1996).
47. Kresse, Georg, and Jürgen Hafner. Ab initio molecular-dynamics simulation of the liquid-metal–amorphous-semiconductor transition in germanium. *Phys. Rev. B* **49,** 14251–14269 (1994).
48. Perdew, John P., et al. Atoms, molecules, solids, and surfaces: Applications of the generalized gradient approximation for exchange and correlation. *Phys. Rev. B* **46**, 6671–6687, (1992).
49. Blöchl, Peter E. "Projector augmented-wave method. *Phys. Rev. B* **50**.17953–17979 (1994).
50. Monkhorst, Hendrik J., and James D. Pack. Special points for Brillouin-zone integrations. *Phys. Rev. B 13*. 5188–5192 (1976).
51. Maintz, Stefan, et al. LOBSTER: A tool to extract chemical bonding from plane-wave based DFT. *J. Comput. Chem.* **37** 1030–1035 (2016).

Schemes

Scheme 1 is available in the Supplementary Files section

Figures

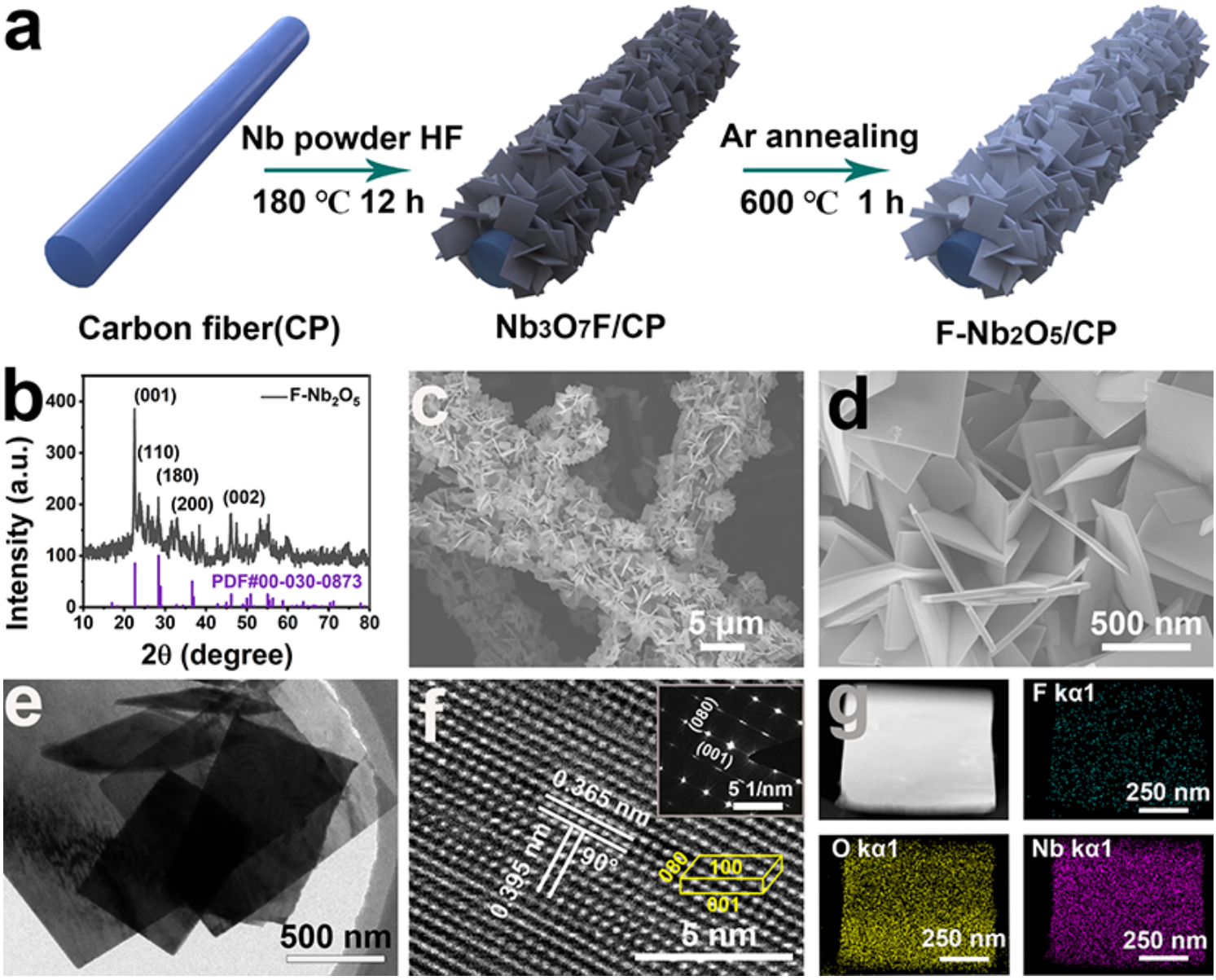

Figure 1

a Schematic illustration of the synthesis of F-Nb_2O_5/CP catalysts. **b** XRD patterns of F-Nb_2O_5. **c** and **d** SEM image of the F-Nb_2O_5/CP. **e** TEM image, **f** HRTEM image, and **g** HAADF-STEM image and corresponding EDS elemental mapping of the F-Nb_2O_5 nanosheets.

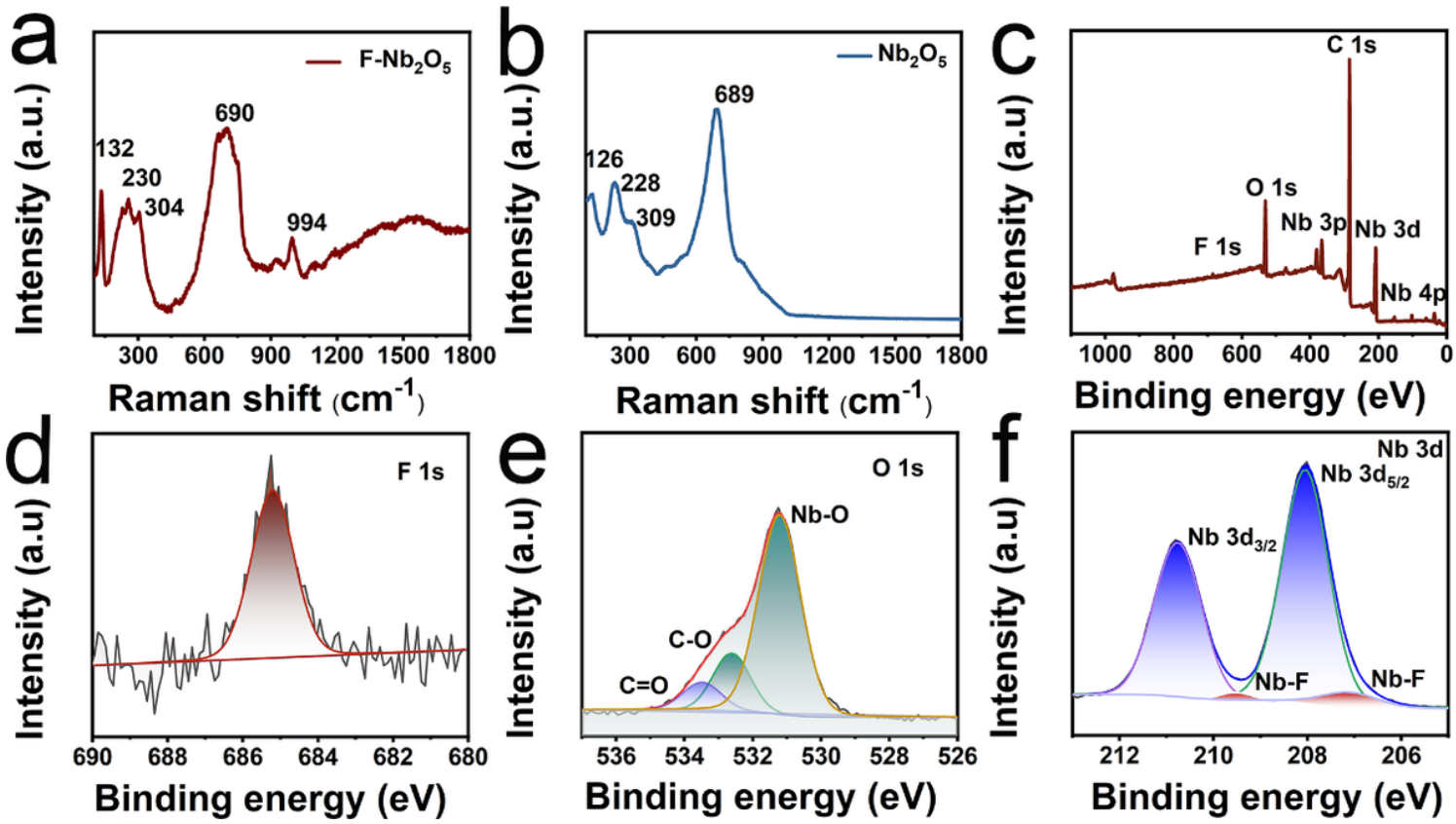

Figure 2

a Raman spectra of F-Nb_2O_5/CP catalyst. **b** Raman spectra of Nb_2O_5. **c** XPS Survey spectrum of F-Nb_2O_5/CP catalysts. High-resolution XPS spectra of **d** F 1s and **e** O 1s and **f** Nb 3d of F-Nb_2O_5/CP catalysts.

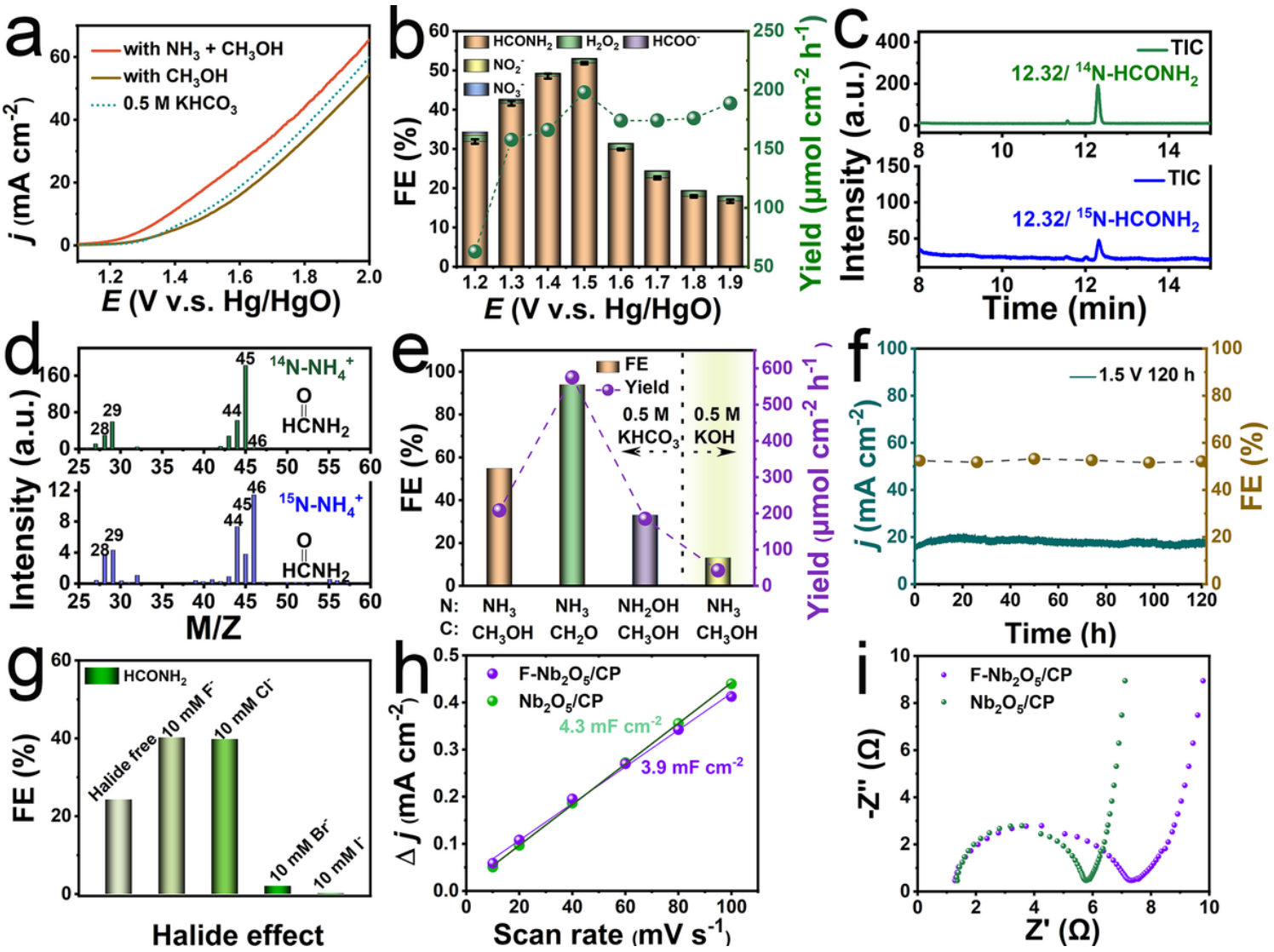

Figure 3

a LSV curves of F-Nb_2O_5/CP in 0.5 M $KHCO_3$ solution, with methanol and NH_3. **b** FEs of oxidation products on F-Nb_2O_5/CP at different potentials. **c** The total ion chromatography (TIC) of ^{14}N formamide and ^{15}N labeled formamide. **d** Corresponding mass spectra of ^{14}N formamide and ^{15}N labeled formamide. **e** C, N source and electrolyte changed for formamide synthesis. **f** long-term electrolysis test on F-Nb_2O_5/CP. **g** Halide effect on Nb_2O_5/CP for formamide synthesis. **h** The capacitive current densities as a function of scan rates for F-Nb_2O_5/CP and Nb_2O_5/CP. **i** Nyquist plots of F-Nb_2O_5/CP and Nb_2O_5/CP.

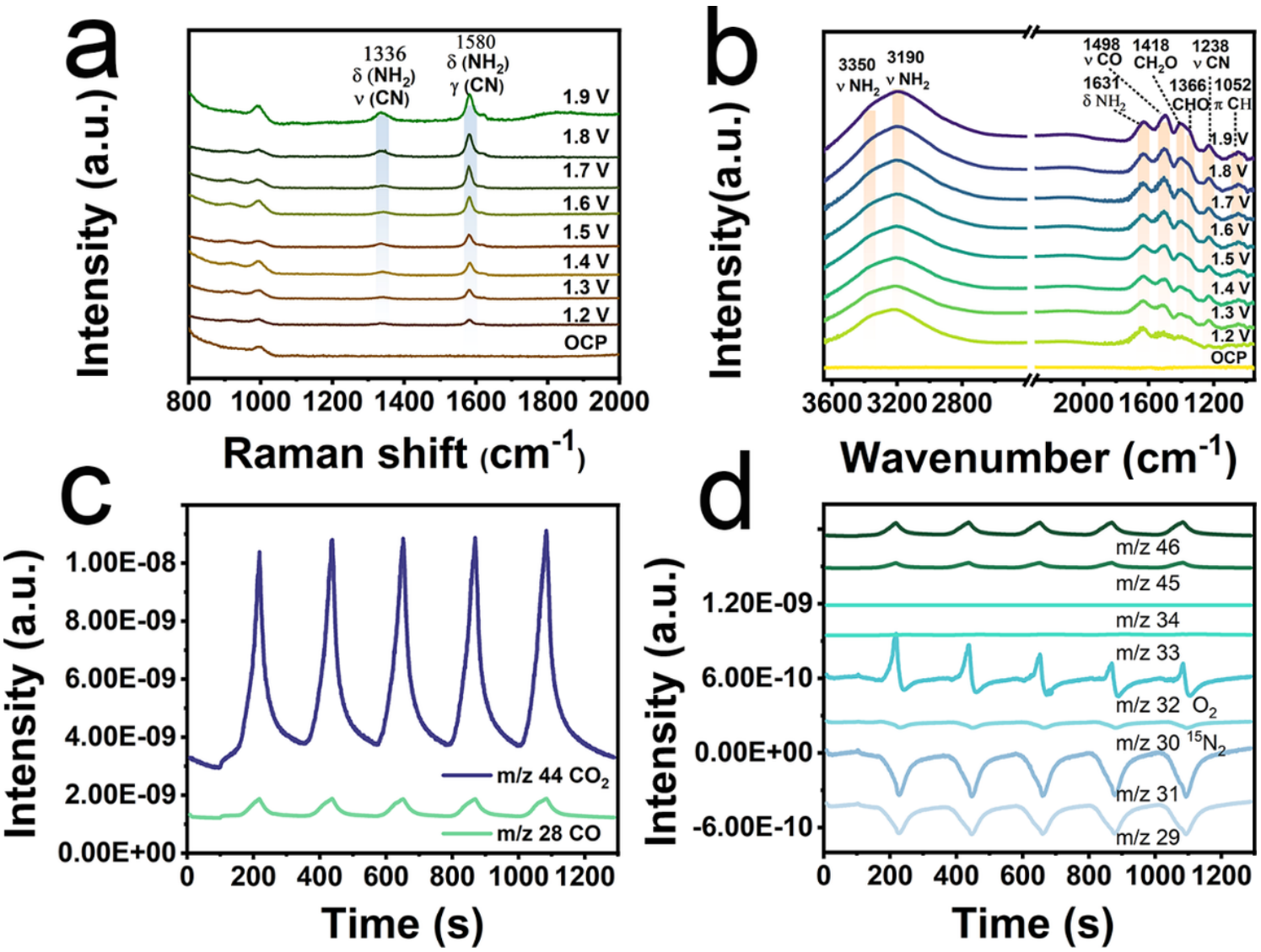

Figure 4

a Potential-dependent in-situ Raman spectra of F-Nb_2O_5/CP catalyst for formamide synthesis. **b** Potential-dependent in situ FTIR-ATR spectra of F-Nb_2O_5/CP catalyst for formamide synthesis. Real-time online DEMS for **c** CO_2, CO products, and **d** for other intermediate.

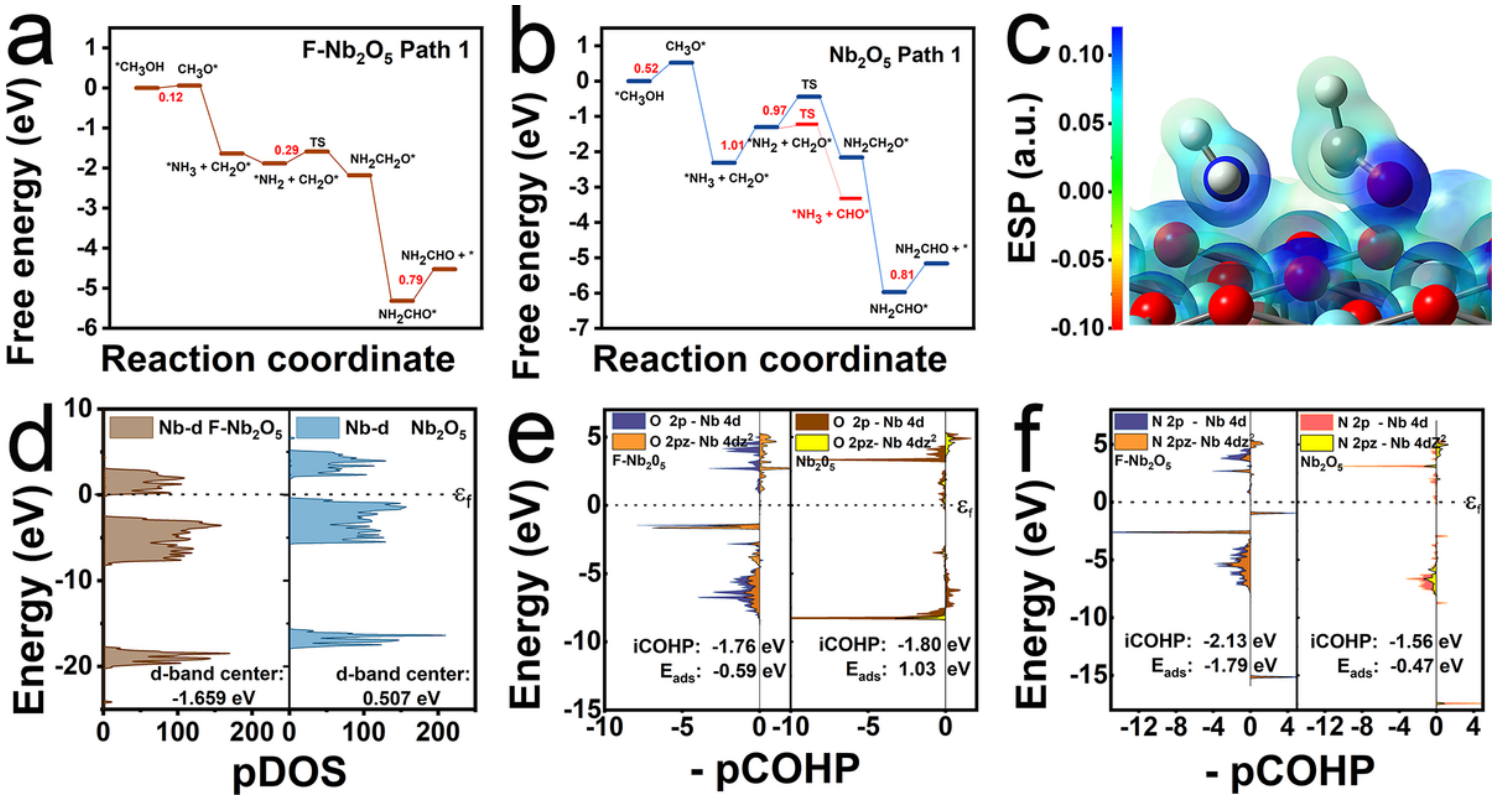

Figure 5

Gibbs free energy diagram of formamide synthesis path 1 on **a** F-Nb_2O_5 (100) surface and **b** Nb_2O_5 (100) surface. Gibbs free energy diagram of formamide synthesis path 2 on **c** The electrostatic potential (ESP) of $^*NH_2$ + $^*CH_2O$. **d** Analysis of projected density of states (pDOS) of Nb-d and corresponding d-band center for F-Nb_2O_5 and Nb_2O_5. **e** COHP analysis of $^*OH^-$ on F-Nb_2O_5 (100) and Nb_2O_5 (100) surface. **f** COHP analysis of $^*NH_2$ on F-Nb_2O_5 (100) and Nb_2O_5 (100) surface.

Supplementary Files

This is a list of supplementary files associated with this preprint. Click to download.

- SupplementaryInformation.docx
- TableofContentsEntry.doc
- Scheme1.png